

# Pressure-induced structural phase transitions in natural kaolinite investigated by Raman spectroscopy and electrical conductivity

MEILING HONG<sup>1,3</sup>, LIDONG DAI<sup>1,2,\*</sup>, HAIYING HU<sup>1,2,\*</sup>, AND XINYU ZHANG<sup>1,3</sup>

<sup>1</sup>Key Laboratory of High-Temperature and High-Pressure Study of the Earth's Interior, Institute of Geochemistry, Chinese Academy of Sciences, Guiyang, Guizhou 550081, China

<sup>2</sup>Shandong Provincial Key Laboratory of Water and Soil Conservation and Environmental Protection, College of Resources and Environment, Linyi University, Linyi, Shandong 276000, China

<sup>3</sup>University of Chinese Academy of Sciences, Beijing 100049, China

## ABSTRACT

We investigated the structural, vibrational, and electrical transport properties of natural kaolinite and its high-pressure polymorphs by Raman scattering and electrical conductivity measurements at 293–673 K and up to 10.0 GPa using diamond-anvil cell. Upon compression, kaolinite underwent two structural transitions from kaolinite I to kaolinite II to kaolinite III phases at pressures of 2.9 and 6.5 GPa, respectively, which was disclosed by the inflection point in the pressure-dependent Raman shifts and electrical conductivity. Upon decompression, kaolinite III directly transformed to kaolinite I at 0.8 GPa without the appearance of kaolinite II. Additionally, the influence of temperature on the structural transformation of natural kaolinite was explored by high-temperature and high-pressure electrical conductivity measurements and negative temperature-dependent transition pressure correlations were obtained. A phase diagram of natural kaolinite was established for the first time and the kaolinite I-kaolinite II and kaolinite II-kaolinite III phase transition boundaries were determined:  $P$  (GPa) =  $4.298 - 0.00462 T$  (K) and  $P$  (GPa) =  $8.895 - 0.00799 T$  (K), respectively. Furthermore, our acquired phase diagram can be applied to understand the stability field of high-pressure polymorphs of kaolinite in the Earth's interior and may provide a phase transition model for other kaolin-group minerals.

**Keywords:** Natural kaolinite, Raman spectroscopy, electrical conductivity, phase diagram, high temperature, high pressure

## INTRODUCTION


As a representative hydrous kaolin-group mineral, kaolinite [ $\text{Al}_2\text{Si}_2\text{O}_5(\text{OH})_4$ ] is widely distributed in the Earth's surface and outcrops in various geotectonic environments (e.g., hydrothermal deposit, altered crustal rock, sedimentary basin, et al.) (Balan et al. 2014; Schroeder and Erickson 2014). Kaolinite is a main component of the oceanic sediment, with its highest content up to 60% (Windom 1976). In addition, kaolinite was also found as the important constituent of sediment in the subduction zone of Earth's mantle, implying that kaolinite has the potential to migrate into the deep Earth interior (Butler and Frost 2006; Sun et al. 2017). Previously available studies also reported that kaolinite plays a crucial role in affecting the water cycle in the deep interior of the Earth and triggering deep-focus volcanism and earthquake (Johnston et al. 2002; Butler and Frost 2006; Hwang et al. 2017). And thus, comprehensive research on the physicochemical behavior for natural kaolinite at high temperature and high pressure is vital to understand its phase stability, storage form, and migration mechanism in the Earth's interior.

Previously available investigations on the phase stabilities and structural transitions for kaolinite at high pressure were performed by synchrotron X-ray diffraction, infrared spectroscopy,

and first-principles theoretical calculations (Mercier and Le Page 2009; Mercier et al. 2010; Welch and Crichton 2010; Welch et al. 2012; Hwang et al. 2017). Two corresponding high-pressure polymorphs of kaolinite have already been identified as kaolinite II phase and kaolinite III phase. Recently, Hwang et al. (2017) revealed that kaolinite I transformed to kaolinite II phase in the pressure range of 3.0–4.0 GPa using synchrotron X-ray diffraction at atmospheric temperature. With increasing pressure, the new kaolinite III phase will appear between 6.0 and 7.0 GPa. Another pressure-induced phase transformation in the natural kaolinite from the Keokuk County, U.S.A., was reported by means of high-pressure synchrotron absorption infrared spectroscopy in transmission mode, and two corresponding transition pressures were determined to be 3.2 and 7.3 GPa, respectively (Welch et al. 2012).

As usual, Raman spectroscopy and electrical conductivity measurements are applied to detect some subtle changes during the pressure-induced structural phase transition. To the best of our knowledge, Raman spectroscopy has been employed to investigate the high-pressure phase transformation of dickite, which is one of the polymorphs for kaolinite at ambient conditions (Johnston et al. 2002). However, no related high-pressure Raman scattering experiment about the structural transition of natural kaolinite was available prior to our study. In regard to the electrical conductivity measurements of kaolinite, previous

\* E-mail: dailidong@vip.gyig.ac.cn and huhaiying@vip.gyig.ac.cn

 Open access: Article available to all readers online.

studies primarily paid attention to its high-temperature electrical transport behavior (Kozík et al. 1992; Trnovcová et al. 2007), and no relevant high-pressure electrical conductivity experiments have been performed. In addition, the influence of temperature on the high-pressure structural transformations of natural kaolinite remains unknown. Therefore, a systematic investigation on Raman scattering and electrical conductivity measurements for natural kaolinite is essential at high temperature and high pressure.

In this study, we report two phase transitions for natural kaolinite at 293–673 K and pressures up to 10.0 GPa using a diamond-anvil cell in conjunction with Raman scattering and alternating current (AC) complex impedance spectroscopy. At each designated pressure condition, the temperature point of phase transition is determined. Furthermore, a phase diagram of natural kaolinite is established in a relatively wide temperature and pressure range, and its possible geological implications are also discussed in detail.

## EXPERIMENTAL PROCEDURES

### Sample preparation and characterization

The natural kaolinite sample used in the experiment was gathered from Nanshu Diggings in Suzhou city, Jiangsu province, China. The initial bulk sample, which is white (Fig. 1), was crushed and ground into micrometer-sized powders using an agate mortar. To determine the crystal structure of the starting sample, X-ray diffraction (XRD) was conducted with a X'Pert Pro X-ray powder diffractometer operating at an accelerating voltage of 45 kV and a beam current of 40 mA. The XRD pattern was used to calculate the lattice constants of the starting sample by Rietveld refinement as implemented in MDI Jade 6.5 software. Figure 1 shows the XRD pattern of the starting sample, and our obtained XRD peaks are in good

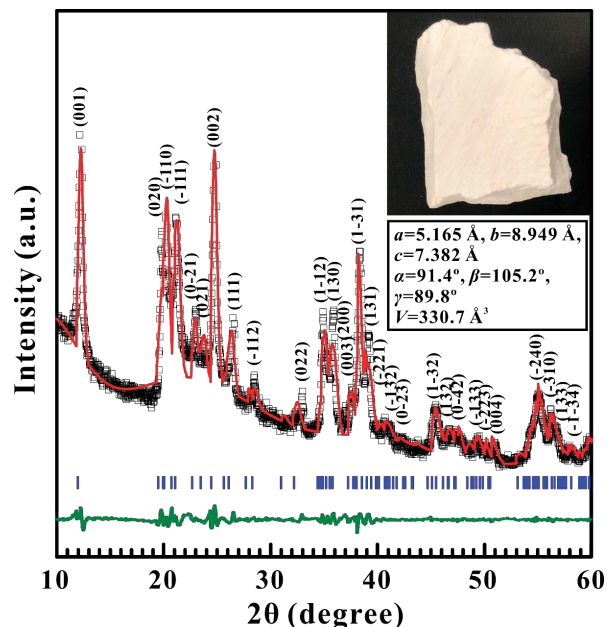


**FIGURE 1.** Rietveld refinement of the diffraction pattern for starting natural kaolinite. Inset: The optical microscope image and the calculated lattice constants for the starting sample. The black open square stands for the observed diffraction pattern and the red solid line represents the calculated diffraction pattern, the blue line is the standardized diffraction peak positions of kaolinite, and the green line below the patterns is the deviation curve between the observed and calculated diffraction patterns.

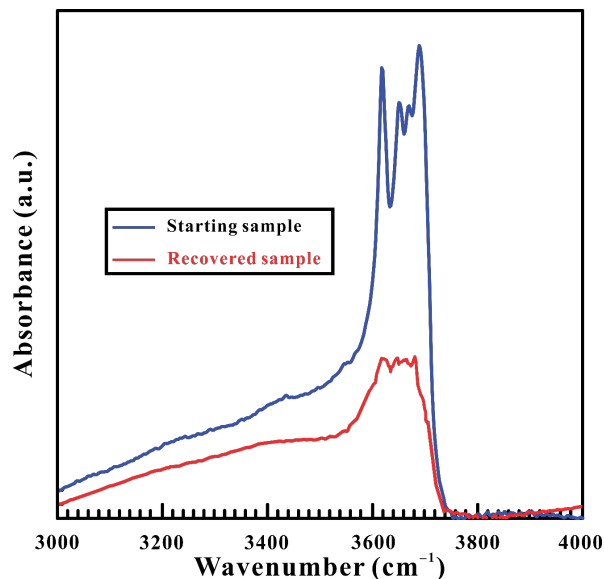


**FIGURE 2.** Representative FTIR spectra of the starting and recovered samples within the wavenumber range of 3000–4000  $\text{cm}^{-1}$ .

agreement with triclinic kaolinite at ambient condition (space group:  $C1$ , JCPDS no. 14-0164). The absence of traces of extra impurity lines in the X-ray diffraction provides robust evidence for the high purity of this natural kaolinite. The lattice constants of natural kaolinite were determined to be  $a = 5.165 \text{ \AA}$ ,  $b = 8.949 \text{ \AA}$ ,  $c = 7.382 \text{ \AA}$ ,  $\alpha = 91.4^\circ$ ,  $\beta = 105.2^\circ$ ,  $\gamma = 89.8^\circ$ , and  $V = 330.7 \text{ \AA}^3$ , which are close to the values in the International Centre for Diffraction Data (ICDD). To check the hydroxyl stretching peaks of natural kaolinite, Fourier transform infrared (FTIR) analysis for the starting sample and the recovered sample decompressed from the highest pressure of 9.5 GPa was performed in the Key Laboratory of High-Temperature and High-Pressure Study of the Earth's Interior, Institute of Geochemistry, Chinese Academy of Sciences, Guiyang, China. The FTIR absorption measurement was carried out with unpolarized radiation from a tungsten light source, a MCT detector with a  $100 \times 100 \text{ \mu m}$  aperture, and a  $\text{CaF}_2$  beam splitter. The spectrum was collected within the wavenumber range of 3000–4000  $\text{cm}^{-1}$  and with 512 scans accumulated for each sample. The representative FTIR spectra for the initial and recovered samples are shown in Figure 2. Four evident characteristic peaks for the initial sample were observed at 3617.5, 3652.2, 3669.5, and 3688.8  $\text{cm}^{-1}$ , respectively, which is also close to the recovered sample at the peak positions of 3619.4, 3650.3, 3667.6, and 3685.0  $\text{cm}^{-1}$ , respectively. All of them are consistent with previous studies (Welch et al. 2012; Balan et al. 2014).

### High-pressure Raman spectroscopy experiments

High-pressure Raman spectroscopy experiments were implemented through a diamond-anvil cell (DAC) with the anvil culet of 300  $\text{\mu m}$ . A ruby single crystal with a grain size of  $\sim 5 \text{ \mu m}$  was chosen to calibrate the pressure by the shift of the R1 fluorescence peak and the uncertainty of pressure calibration is  $< 5\%$ . In this study, a mixture of methanol and ethanol (4:1 volume ratio) was used as the pressure medium to provide hydrostatic conditions and no pressure medium was adopted to create non-hydrostatic conditions. High-pressure Raman spectra were performed using a Renishaw 2000 micro confocal Raman spectrometer equipped with a near infrared (IR) 785 nm diode laser device. Raman spectra were gathered within the wavenumber ranges of 100–1000 and 3500–3800  $\text{cm}^{-1}$  so as to identify the lattice vibrational and hydroxyl stretching modes of kaolinite, respectively. To avoid pressure fluctuations, an equilibration time of 15 min was maintained at each predesigned pressure point. Furthermore, the positions of Raman peaks were determined by fitting the Lorentz-type function using PeakFit software.

### High-temperature and high-pressure electrical conductivity measurements

The DAC having a couple of anvil culet of 300  $\text{\mu m}$  was utilized for high-temperature and high-pressure electrical conductivity measurements. High temperature

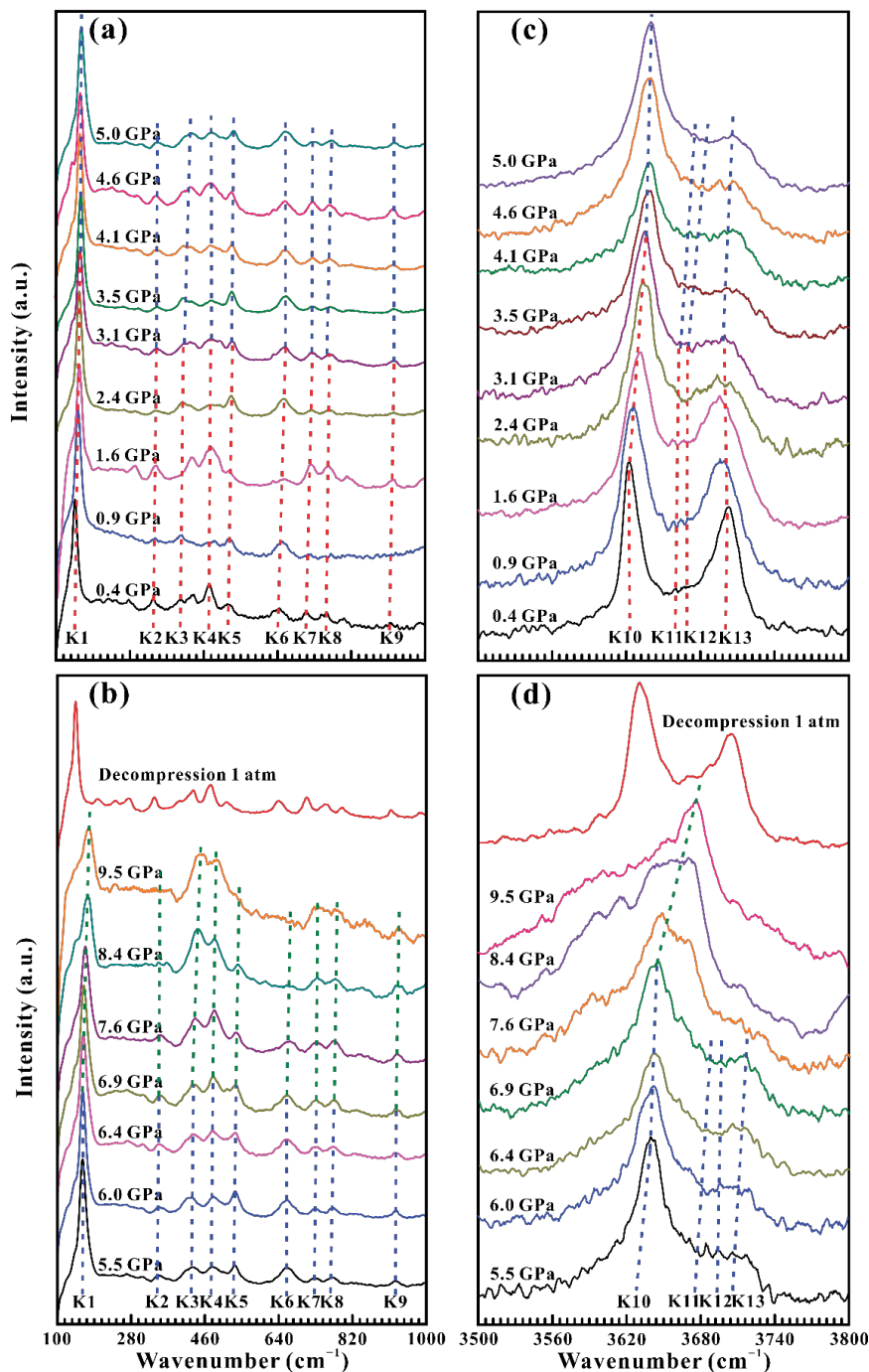


**FIGURE 3.** Raman spectra of natural kaolinite in the pressure range of 0.4–9.5 GPa during compression and the Raman spectrum of kaolinite decompression to 1 atm under non-hydrostatic condition. In here, (a and b) the lattice vibrational mode (100–1000  $\text{cm}^{-1}$ ) and (c and d) the hydroxyl stretching mode (3500–3800  $\text{cm}^{-1}$ ), respectively.

was provided by two external electric resistance heating furnaces placed around the diamond anvil and the temperature was monitored using a K-type thermocouple with the error of  $\pm 5$  K. A T-301 stainless steel gasket was pre-indented into a thickness of  $\sim 40$   $\mu\text{m}$  and later a 180  $\mu\text{m}$  center hole was drilled by a laser drilling machine. Subsequently, a mixture of boron nitride and epoxy powder was compressed into the hole and another 100  $\mu\text{m}$  center hole was drilled as the insulating

sample chamber. The AC complex impedance spectroscopy measurements were carried out by the two-electrode method using a Solartron-1260 impedance/gain phase analyzer within the predetermined frequency range of  $10^{-1}$ – $10^7$  Hz and at a signal voltage of 1.0 V. More detailed descriptions of the high-pressure experimental technique and measurement procedures were reported elsewhere (Dai et al. 2016, 2017, 2018, 2019; Zhuang et al. 2017; Yang et al. 2021).

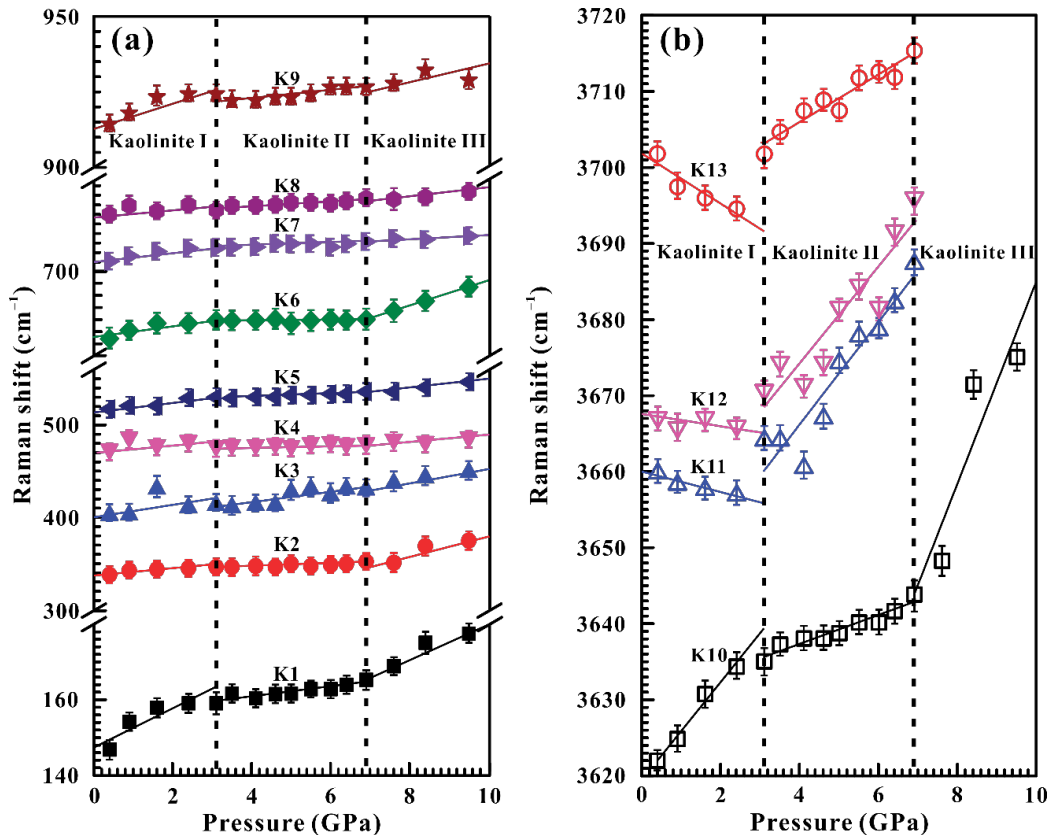


FIGURE 4. Pressure dependence the Raman shift with increasing pressure for natural kaolinite under non-hydrostatic condition. In here, (a) stands for the lattice vibrational mode (100–1000  $\text{cm}^{-1}$ ), (b) represents the hydroxyl stretching mode (3500–3800  $\text{cm}^{-1}$ ), respectively.

## RESULTS AND DISCUSSION

### Two phase transitions of natural kaolinite at room temperature

High-pressure Raman spectroscopy was performed to investigate the vibrational property of natural kaolinite up to 9.5 GPa at room temperature. As shown in Figure 3a, nine Raman-active modes of natural kaolinite are observed within the wavenumber range of 100–1000  $\text{cm}^{-1}$  at the pressure of 0.4 GPa under non-hydrostatic conditions. The sharp peak at 146.8  $\text{cm}^{-1}$  (denoted as K1 mode in Fig. 3a) is the characteristic peak of kaolinite, which can be ascribed to the O-Al-O symmetric bending mode. Four Raman peaks at 337.8, 402.4, 473.6, and 517.2  $\text{cm}^{-1}$  (expressed as K2, K3, K4, and K5 modes) are assigned to the O-Si-O bending modes. The Raman peak at 644.2  $\text{cm}^{-1}$  (denoted as K6 mode) is attributed to the Al-OH translational vibration. Two Raman peaks at 710.9 and 759.9  $\text{cm}^{-1}$  (marked as K7, K8 modes) are related to the hydroxyl translational vibration caused by the flexing of O-Si-O bond. The Raman peak at 914.3  $\text{cm}^{-1}$  (denoted as K9 mode) originates from the inner hydroxyl deformation. At the same time, four representative hydroxyl stretching peaks at 3622.0, 3659.9, 3670.0, and 3701.8  $\text{cm}^{-1}$  (denoted as K10, K11, K12, and K13 modes in Fig. 3c) are detected within the wavenumber range of 3500–3800  $\text{cm}^{-1}$ . The Raman peak at 3622.0  $\text{cm}^{-1}$  comes from the stretching vibration of the inner

hydroxyl, whereas the other three Raman peaks are correspondent to the inner surface hydroxyl stretching vibration. All of these obtained Raman peaks coincide with prior studies (Frost 1995, 1997; Frost et al. 1999; Zhang et al. 2014; Samyn et al. 2015).

The pressure dependence of Raman shift (pressure coefficient,  $d\omega/dP$ , in here,  $\omega$  and  $P$  are the Raman shift and pressure, respectively) and its corresponding fitting results for natural kaolinite under non-hydrostatic conditions are displayed in Figure 4 and

TABLE 1. Pressure dependence of the Raman shift ( $d\omega/dP$ ) ( $\text{cm}^{-1} \text{GPa}^{-1}$ ) for natural kaolinite under non-hydrostatic condition

Pressure (GPa)	$\omega$ ( $\text{cm}^{-1}$ )	$d\omega/dP$ ( $\text{cm}^{-1} \text{GPa}^{-1}$ )	$\omega$ ( $\text{cm}^{-1}$ )	$d\omega/dP$ ( $\text{cm}^{-1} \text{GPa}^{-1}$ )	$\omega$ ( $\text{cm}^{-1}$ )	$d\omega/dP$ ( $\text{cm}^{-1} \text{GPa}^{-1}$ )
0.4–2.4	146.8 (K1)	5.79	644.2 (K6)	6.27	3659.9 (K11)	-1.36
	337.8 (K2)	3.21	710.9 (K7)	6.68	3670.0 (K12)	-1.71
	402.4 (K3)	7.32	759.9 (K8)	3.58	3701.8 (K13)	-3.31
	473.6 (K4)	2.61	914.3 (K9)	5.14		
	517.2 (K5)	5.32	3622.0 (K10)	6.40		
3.1–6.4	159.1 (K1)	1.17	659.2 (K6)	0.059	3664.2 (K11)	6.74
	346.2 (K2)	0.99	724.6 (K7)	1.04	3670.7 (K12)	6.34
	413.2 (K3)	6.34	764.5 (K8)	2.15	3701.8 (K13)	3.13
	477.1 (K4)	0.98	924.3 (K9)	1.09		
	530.1 (K5)	1.39	3635.1 (K10)	1.90		
6.9–9.5	165.3 (K1)	4.87	660.3 (K6)	10.16	3687.4 (K11)	-
	352.2 (K2)	10.01	731.5 (K7)	1.86	3696.0 (K12)	-
	429.8 (K3)	7.17	777.0 (K8)	2.79	3715.4 (K13)	-
	480.7 (K4)	1.84	926.6 (K9)	1.12		
	535.9 (K5)	4.34	3643.9 (K10)	13.30		

Note: In here,  $\omega$  ( $\text{cm}^{-1}$ ) and  $P$  (GPa) are the Raman shift and pressure, respectively.

Table 1. As seen from Figure 4a, all of the Raman peaks in the lattice vibrational range ( $100\text{--}1000\text{ cm}^{-1}$ ) monotonously tend to move toward higher wavenumbers with the rise of pressure. However, we can distinguish three representative pressure regions based on the variation of the pressure-dependent Raman shift ( $d\omega/dP$ ): from 0.4 to 2.4 GPa, from 3.1 to 6.4 GPa, and as well as from 6.9 to 9.5 GPa, respectively. Below 3.1 GPa, K1, K2, K5, and K6 modes move rapidly toward higher wavenumbers with increasing pressure at  $5.79$ ,  $3.21$ ,  $5.32$ , and  $6.27\text{ cm}^{-1}\text{ GPa}^{-1}$ , respectively. However, within the pressure range of 3.1–6.4 GPa, relatively smaller pressure coefficients of  $1.17$ ,  $0.99$ ,  $1.39$ , and  $0.059\text{ cm}^{-1}\text{ GPa}^{-1}$  are obtained for K1, K2, K5, and K6 modes, respectively. When the pressure is higher than 6.9 GPa, K1, K2, K5, and K6 modes shift toward higher wavenumbers with larger pressure coefficients of  $4.87$ ,  $10.01$ ,  $4.34$ , and  $10.16\text{ cm}^{-1}\text{ GPa}^{-1}$ . In regard to the hydroxyl stretching modes ( $3500\text{--}3800\text{ cm}^{-1}$ ) of natural kaolinite, below 3.1 GPa, the K10 mode shifts toward a higher wavenumber with a rapid rate of  $6.40\text{ cm}^{-1}\text{ GPa}^{-1}$ , while K11, K12m and K13 modes show red shifts with the separate

rates of  $-1.36$ ,  $-1.71$ , and  $-3.31\text{ cm}^{-1}\text{ GPa}^{-1}$ . Within the pressure range of 3.1–6.4 GPa, the K10 mode exhibits a blue shift with a relatively lower rate of  $1.90\text{ cm}^{-1}\text{ GPa}^{-1}$ , whereas K11, K12, and K13 modes change their pressure coefficients from negative to positive and shift toward higher wavenumbers with higher rates of  $6.74$ ,  $6.34$ , and  $3.13\text{ cm}^{-1}\text{ GPa}^{-1}$ , respectively. Above 6.9 GPa, the K10 mode continuously shifts toward higher wavenumber with a rapid rate of  $13.30\text{ cm}^{-1}\text{ GPa}^{-1}$ , while the remaining Raman peaks of sample disappear. All of this above-mentioned evidence, including the apparent discontinuity in pressure coefficients for K1, K2, K5, K6, and K10 modes, the conversion of pressure coefficients from negative to positive for K11, K12, and K13 modes, and as well as the disappearance of K11, K12, and K13 modes, disclose the occurrence of kaolinite I-kaolinite II and kaolinite II-kaolinite III structural transitions at 3.1 and 6.9 GPa, respectively. Upon further compression above 7.6 GPa, the Raman peak intensity of the sample decreased significantly, which may be caused by the destruction of the crystal structure under high pressure (Laiglesia 1993; Galán et al. 2006). After

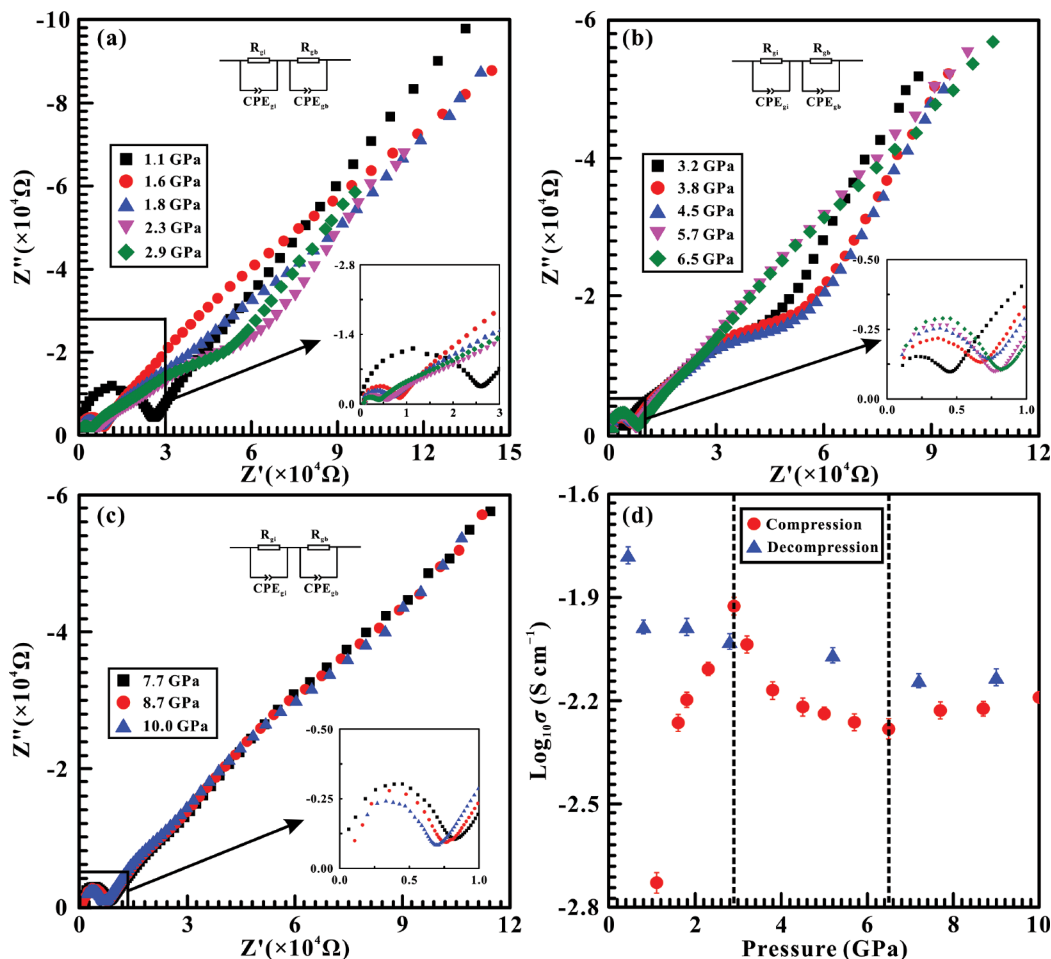


**FIGURE 5.** (a–c) Impedance spectra of natural kaolinite at the pressure range of 1.1–10.0 GPa and atmospheric temperature in the process of compression.  $Z'$  and  $Z''$  are the real and imaginary parts of complex impedance, respectively. The equivalent circuit consisted of the series connection of  $R_{gi}$ - $CPE_{gi}$  and  $R_{gb}$ - $CPE_{gb}$  ( $R_{gi}$  and  $CPE_{gi}$  represent the resistance and the constant phase element of grain interior, respectively;  $R_{gb}$  and  $CPE_{gb}$  are the resistance and the constant phase element of grain boundary, respectively). (d) Pressure-dependent electrical conductivity for natural kaolinite during compression and decompression at atmospheric temperature.

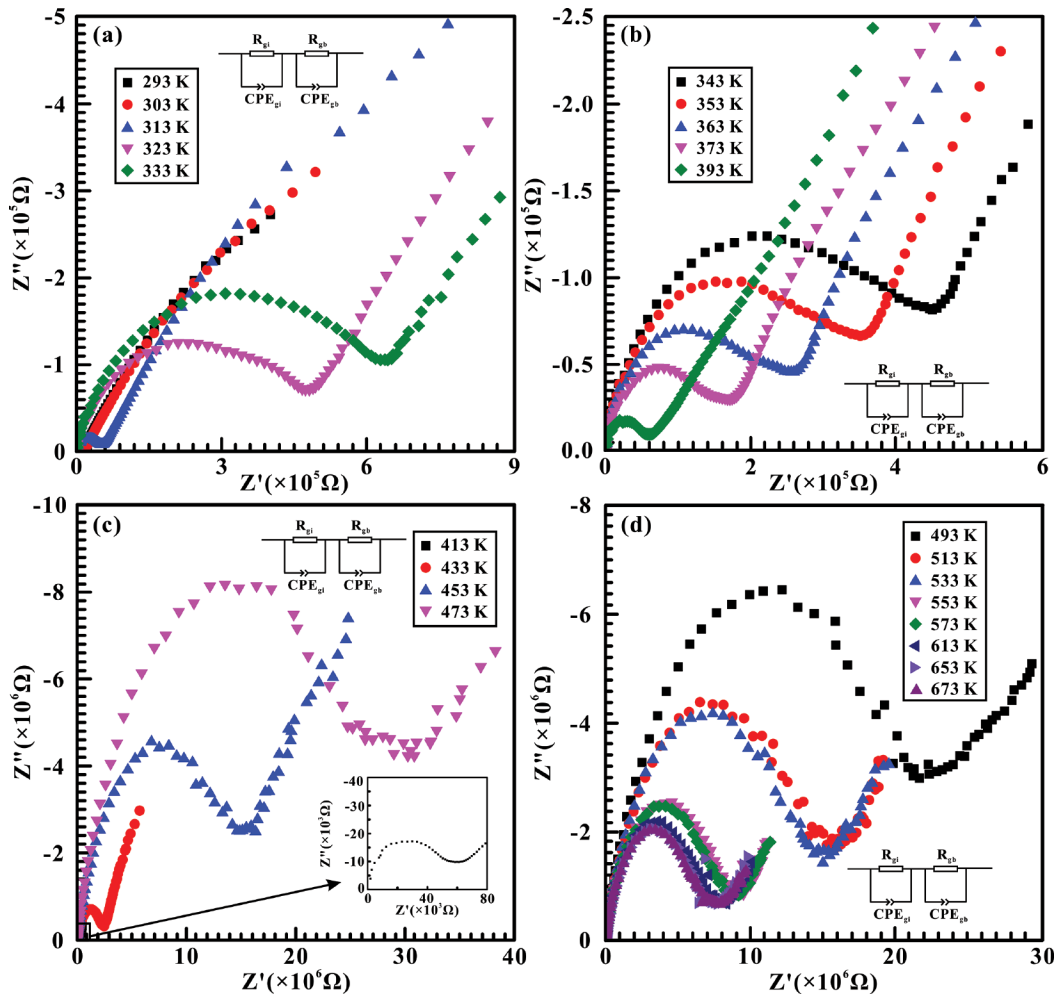


FIGURE 6. Representative complex impedance spectra of natural kaolinite at a pressure of 2.3 GPa and temperature ranges of (a) 293–333 K, (b) 343–393 K, (c) 413–473 K, and (d) 493–673 K, respectively.

quenching to ambient conditions, the obtained Raman spectroscopy can be recovered to its initial state, which suggests a direct structural transition from kaolinite III to kaolinite I phases. The recoverability of kaolinite I phase after decompression to ambient conditions was also confirmed by our FTIR spectra results (Fig. 2). As for the high-pressure Raman spectroscopy of natural kaolinite under hydrostatic conditions (Online Material<sup>1</sup> Figs. OM1 and OM2; Online Material<sup>1</sup> Table OM1), similar phase transformation pressure points are acquired at 2.9 and 6.7 GPa, respectively. And thus, the influence of different hydrostatic environments on the pressures of phase transitions for natural kaolinite can be ignored.

Representative Nyquist diagrams of the impedance spectroscopy for natural kaolinite at atmospheric temperature during compression are illustrated in Figures 5a–5c. The impedance spectra exhibit an approximate semicircle within the high-frequency regime and a low-frequency oblique line. To determine the electrical resistance results from the impedance spectroscopy data, each impedance semicircular arc of natural kaolinite was simulated by an equivalent circuit composed of a parallel

resistor (R) and constant-phase element (CPE). All the fitting errors were <5% of the electrical resistance. Figure 5d displays the relation between electrical conductivity and pressure for natural kaolinite in the processes of compression and decompression. According to the pressure-dependent electrical conductivity slopes, we divided the compression process into three diverse pressure ranges. Below 2.9 GPa, the electrical conductivity of sample enhances rapidly with increasing pressure at a rate of  $0.40 \text{ S cm}^{-1} \text{ GPa}^{-1}$ . However, an opposite pressure-dependent electrical conductivity variation trend is detected within the pressure range of 2.9–6.5 GPa. A notable discontinuity in electrical conductivity at 2.9 GPa indicates the structural transformation from kaolinite I to kaolinite II phases. On further compression above 6.5 GPa, the electrical conductivity of sample increases slightly with the rise of pressure at a rate of  $0.025 \text{ S cm}^{-1} \text{ GPa}^{-1}$ . The discontinuous change in electrical conductivity at 6.5 GPa is consistent with our above-mentioned Raman scattering results and can be attributed to the kaolinite II-kaolinite III phase transition. In the process of decompression, the negative dependence of electrical conductivity on pressure at a rate of  $-0.021 \text{ S cm}^{-1}$

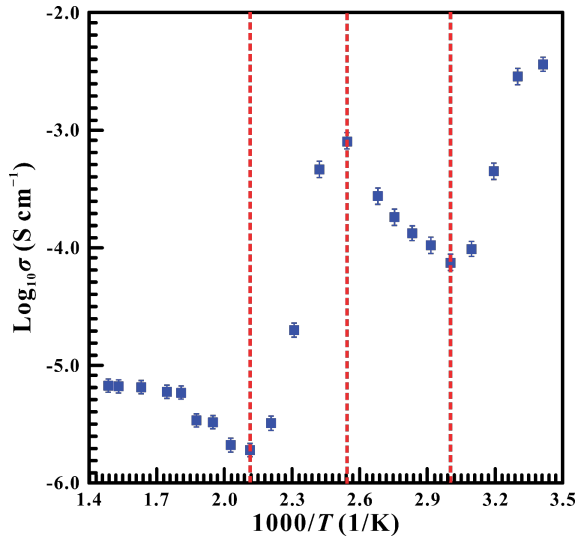


FIGURE 7. Logarithm of electrical conductivity against the reciprocal of temperature for kaolinite I at 2.3 GPa and 293–673 K.

GPa<sup>-1</sup> is obtained above 0.8 GPa. As the pressure decreased from 0.8 to 0.4 GPa, the logarithmic electrical conductivity of sample increases from -1.99 to -1.78 S cm<sup>-1</sup>. An inflection point in electrical conductivity at 0.8 GPa can be ascribed to the direct structural transformation from kaolinite III to kaolinite I.

**Two phase transitions of natural kaolinite at high temperature**

Temperature is an important factor in influencing the phase transition pressure for some hydrous minerals and rocks (e.g., Ono 1998; Hu et al. 2017, 2018; Sun et al. 2017). To illustrate the effect of temperature on the phase transition pressure of kaolinite, a series of electrical conductivity measurements were implemented at pressures of 1.7, 2.3, 4.0, 5.0, and 8.0 GPa and temperature range of 293–673 K.

Representative impedance spectroscopy results of natural kaolinite at 2.3 GPa and a temperature range of 293–673 K are shown in Figure 6. The relationship between logarithmic electrical conductivity and reciprocal temperature for natural kaolinite is displayed in Figure 7. At 293–333 K, the electrical conductivity of kaolinite decreases with the rise of temperature.

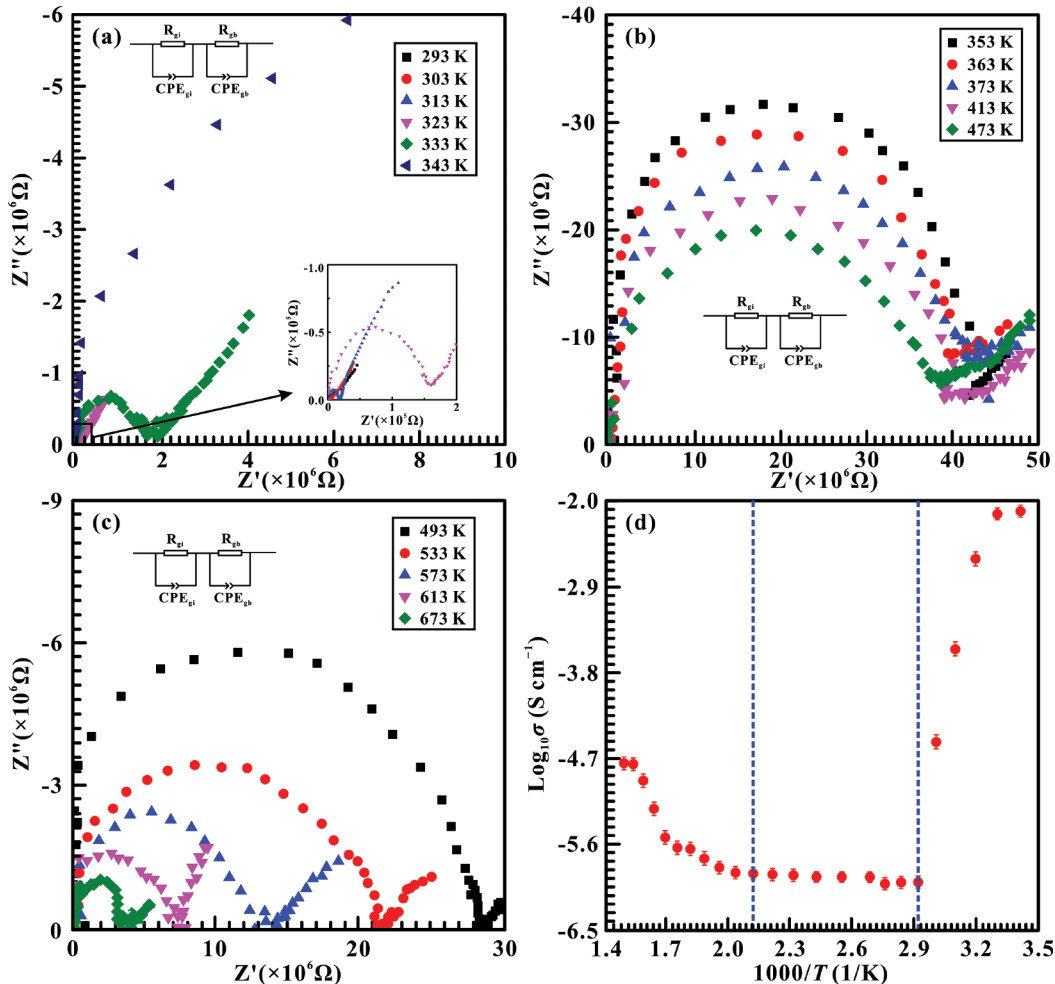
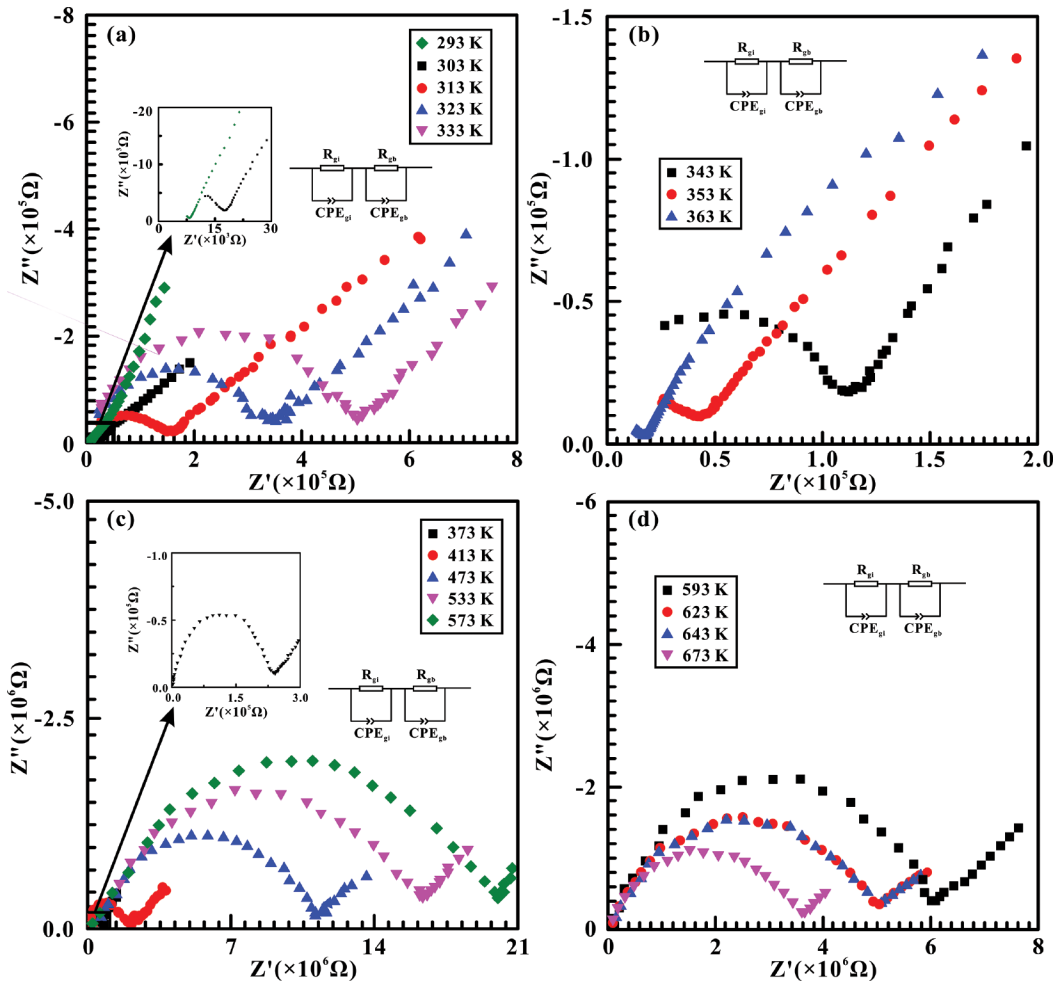


FIGURE 8. (a–c) Nyquist diagrams of impedance spectroscopy for kaolinite III at 8.0 GPa over the temperature range of 293–673 K. (d) The correspondent temperature-dependent electrical conductivity relationship.



**FIGURE 9.** Typical complex impedance spectra of kaolinite II at a given pressure of 4.0 GPa and temperature ranges of (a) 293–333 K, (b) 343–363 K, (c) 373–573 K, and (d) 593–673 K, respectively.

Previous thermogravimetric investigations have revealed that kaolinite released physically bonded water (PBW, i.e., the polar water molecules that are bonded to the surface of pores and defect sites of crystals) in the temperature range of 293–338 K (Cheng et al. 2010; Kubliha et al. 2017). Thus, our observed negative temperature-dependent electrical conductivity correlation at 293–333 K is probably associated with the removal of PBW. In the temperature ranges of 333–393 and 473–673 K, the electrical conductivity of sample increases with increasing temperature, which can be ascribed to the increased mobility of charge carriers at higher temperatures (Kozík et al. 1992; Trnovcová et al. 2007). However, we found that the electrical conductivity of sample diminishes drastically, by about three orders of magnitude, at 393–473 K, which possibly results from the structural transition from kaolinite I to kaolinite II phases. To verify the hypothesis of the occurrence of a phase transition at 393–473 K and 2.3 GPa, a new high-temperature electrical conductivity measurement was carried out for kaolinite III at 8.0 GPa, as shown in Figure 8. According to our high-pressure Raman scattering results, no structural transformation was detected for kaolinite III phase up to the highest pressure of 9.5 GPa. Besides,

our obtained high-temperature electrical conductivity variation tendency of kaolinite III is analogous to previously reported results for kaolinite I where no structural transition occurred (Kozík et al. 1992; Trnovcová et al. 2007). And thus, the same electrical conductivity variation mechanisms may operate in the high-pressure polymorph of kaolinite without a phase transition (Kozík et al. 1992; Trnovcová et al. 2007) (i.e., the negative temperature-dependent electrical conductivity relationship at low temperature arises from the removal of PBW and the positive temperature-dependent electrical conductivity correlation at middle and high-temperature regions is due to the increased mobility of charge carriers). Therefore, kaolinite III provides a reference of no phase transition for kaolinite I and kaolinite II. We compared the electrical conductivity results at 2.3 GPa with that at 8.0 GPa and found that the first drop of electrical conductivity occurs in approximately the same temperature range. In the temperature range of 343–473 K, the electrical conductivity of kaolinite III increases slightly with increasing temperature, while a more rapid increase in electrical conductivity is detected for kaolinite I at 333–393 K followed by a dramatic decrease at 393–473 K. When the temperature is higher than 473 K, both



kaolinite I and kaolinite III show positive temperature-dependent electrical conductivity relationships. Thus, we conclude that the abnormal drop in electrical conductivity observed at 393–473 K and 2.3 GPa is attributed to the kaolinite I–kaolinite II phase transformation. Furthermore, the high-temperature electrical conductivity result at 1.7 GPa is similar to that at 2.3 GPa, with a significant decrease in electrical conductivity at 413–533 K due to the appearance of kaolinite II.

To elucidate the relationship between temperature and the structural transition pressure of kaolinite II and kaolinite III, electrical conductivity measurements were conducted at pressures of 2.9–6.5 GPa and temperatures of 293–673 K. Typical Nyquist diagrams of kaolinite II phase measured at 4.0 GPa and 293–673 K are shown in Figure 9. The logarithmic electrical conductivity of kaolinite II as a function of reciprocal temperature is displayed in Figure 10. Comparing the high-temperature electrical conductivity results of kaolinite II with that of kaolinite III, an apparent decrease in electrical conductivity at 363–573 K for kaolinite II is observed and suggests the structural transformation from kaolinite II to kaolinite III. At 5.0 GPa, a similar phenomenon of a remarkable decrease in electrical conductivity is also detected in the temperature range of 373–533 K, which provides a clear clue for the occurrence of kaolinite III. On the other hand, by comparing the high-temperature electrical conductivity data at different pressures, we found that the influence of temperature on the electrical conductivity of kaolinite is much more pronounced than that of pressure, which is consistent with previous studies for hydrous silicate minerals and rocks (Hu et al. 2017, 2018).

On the basis of the phase transition pressures and temperatures obtained from electrical conductivity measurements, we can establish a  $P$ - $T$  phase diagram for natural kaolinite in a relatively wide pressure range from 1.7 to 6.5 GPa and temperature range of 293–673 K, as displayed in Figure 11. According to the phase diagram of natural kaolinite, the kaolinite I to kaolinite II and

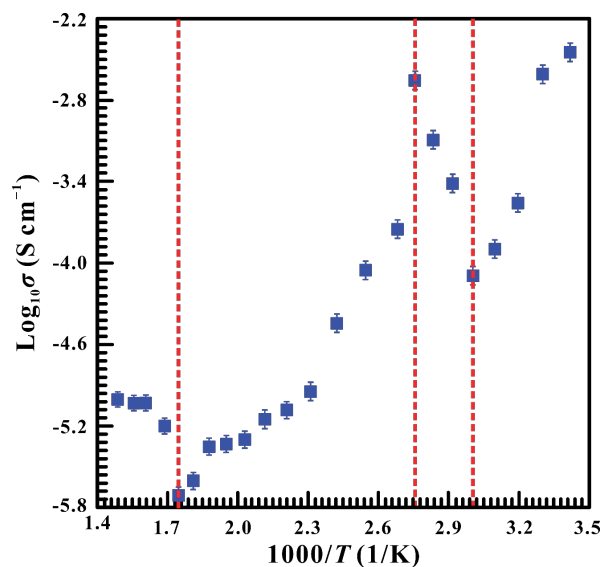


**FIGURE 10.** Logarithmic electrical conductivity of kaolinite II as a function of reciprocal temperature under the conditions of 4.0 GPa and 293–673 K.

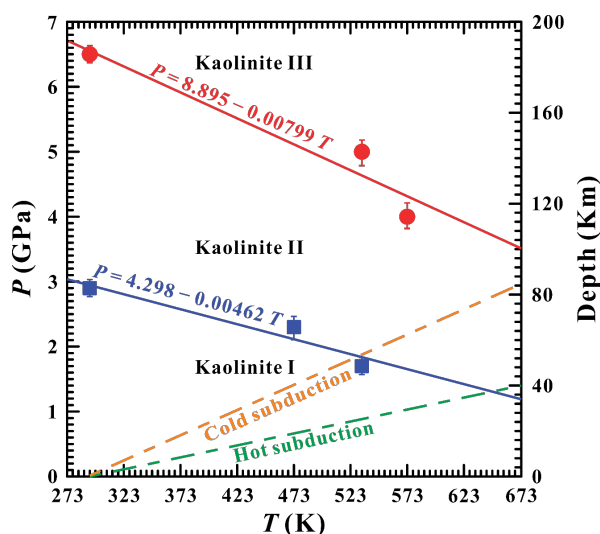


**FIGURE 11.** Proposed  $P$ - $T$  phase diagram of natural kaolinite investigated at pressures up to 6.5 GPa and temperatures up to 673 K. Blue and red solid lines represent the structural transition boundaries of kaolinite I–kaolinite II and kaolinite II–kaolinite III phases, respectively. The orange and green dashed lines stand for the cold and hot subduction zones with the geothermal gradient of 5 and 10 K km<sup>-1</sup>, respectively.

kaolinite II to kaolinite III phase transformation boundaries can be described as  $P$  (GPa) = 4.298 – 0.00462  $T$  (K) and  $P$  (GPa) = 8.895 – 0.00799  $T$  (K), respectively.

## IMPLICATIONS

Two different experimental methods have been applied to research the structural transitions of natural kaolinite at higher temperatures and pressures than prior studies and with broader  $P$ - $T$  coverage (Welch and Crichton 2010; Welch et al. 2012; Hwang et al. 2017). The first quantitative functional relation describing the phase transition temperature and pressure was established for natural kaolinite under the conditions of 1.7–6.5 GPa and 293–673 K. Furthermore, the phase diagram of natural kaolinite can be used to deeply understand its phase stability, storage form, and migration mechanism in the Earth’s interior.

Based on the phase diagram of natural kaolinite, the stability fields of high-pressure polytypes of kaolinite can occur along cold and hot subduction zones (Chen et al. 2013). Along a typical cold subduction path with a geothermal gradient of 5 K km<sup>-1</sup>, kaolinite I remains stable below 2.0 GPa or a depth of 60 km. At depths greater than 60 km, kaolinite II appears. However, along a hot subduction path with the geothermal gradient of 10 K km<sup>-1</sup>, kaolinite I remains stable at a shallower depth of about 40 km than in a cold subduction zone. Kaolinite II forms at depths >40 km. Our results indicate that kaolinite II has the potential to enter the mantle through both cold and hot subduction zones and serves as a source of aluminum, silicon, and hydrogen to the Earth’s interior.

It is well known that kaolin-group minerals share the same structural units consisting of a [SiO<sub>4</sub>] tetrahedral and an [AlO<sub>6</sub>] octahedral layer but differ in the stacking of layers (Balan et al. 2014). Furthermore, a similar layer slipping mechanism was

found in the pressure-induced structural transition of dickite along with kaolinite and appears to be a general high-pressure transition mechanism among kaolin-group minerals (Dera et al. 2003). And thus, our phase diagram of natural kaolinite can be regarded as a model system for other kaolin-group minerals.

#### ACKNOWLEDGMENTS AND FUNDING

Some kind guidance and helps from Heping Li in the Key Laboratory of High-Temperature and High-Pressure Study of the Earth's Interior, Institute of Geochemistry, Chinese Academy of Sciences are obtained for the in situ high-pressure Raman scattering measurements. This research was financially supported by the NSF of China (42072055, 41774099, and 41772042), Youth Innovation Promotion Association of CAS (Grant No. 2019390), Special Fund of the West Light Foundation of CAS and as well as Special Fund from Shandong Provincial Key Laboratory of Water and Soil Conservation and Environmental Protection.

#### REFERENCES CITED

- Balan, E., Calas, G., and Bish, D.L. (2014) Kaolin-group minerals: From hydrogen-bonded layers to environmental recorders. *Elements*, 10, 183–188.
- Butler, I.S., and Frost, R.L. (2006) An overview of the high-pressure vibrational spectra of clays and related minerals. *Applied Spectroscopy Reviews*, 41, 449–471.
- Chen, Y., Ye, K., Wu, T.F., and Guo, S. (2013) Exhumation of oceanic eclogites: Thermodynamic constraints on pressure, temperature, bulk composition and density. *Journal of Metamorphic Geology*, 31, 549–570.
- Cheng, H.F., Yang, J., Liu, Q.F., He, J.K., and Frost, R.L. (2010) Thermogravimetric analysis–mass spectrometry (TG-MS) of selected Chinese kaolinites. *Thermochimica Acta*, 507, 106–114.
- Dai, L.D., Wu, L., Li, H.P., Hu, H.Y., Zhuang, Y.K., and Liu, K.X. (2016) Evidence of the pressure-induced conductivity switching of yttrium-doped SrTiO<sub>3</sub>. *Journal of Physics: Condensed Matter*, 28, 475501.
- Dai, L.D., Zhuang, Y.K., Li, H.P., Wu, L., Hu, H.Y., Liu, K.X., Yang, L.F., and Pu, C. (2017) Pressure-induced irreversible amorphization and metallization with a structural phase transition in arsenic telluride. *Journal of Materials Chemistry C*, 5, 12, 157–12, 162.
- Dai, L.D., Liu, K.X., Li, H.P., Wu, L., Hu, H.Y., Zhuang, Y.K., Yang, L.F., Pu, C., and Liu, P.F. (2018) Pressure-induced irreversible metallization accompanying the phase transitions in Sb<sub>2</sub>S<sub>3</sub>. *Physical Review B*, 97, 024103.
- Dai, L.D., Pu, C., Li, H.P., Hu, H.Y., Liu, K.X., Yang, L.F., and Hong, M.L. (2019) Characterization of metallization and amorphization for GaP under different hydrostatic environments in diamond anvil cell up to 40.0 GPa. *Review of Scientific Instruments*, 90, 066103.
- Dera, P., Prewitt, C.T., Japel, S., Bish, D.L., and Johnston, C.T. (2003) Pressure-controlled polytypism in hydrous layered materials. *American Mineralogist*, 88, 1428–1435.
- Frost, R.L. (1995) Fourier transform Raman spectroscopy of kaolinite, dickite and halloysite. *Clays and Clay Minerals*, 43, 191–195.
- (1997) The structure of the kaolinite minerals—a FT-Raman study. *Clay Minerals*, 32, 65–77.
- Frost, R.L., Kristof, J., Horvath, E., and Klopogge, J.T. (1999) Modification of the kaolinite hydroxyl surfaces through the application of pressure and temperature. *Journal of Colloid and Interface Science*, 214, 380–388.
- Galán, E., Aparicio, P., La Iglesia, A., and González, I. (2006) The effect of pressure on order/disorder in kaolinite under wet and dry conditions. *Clays and Clay Minerals*, 54, 230–239.
- Hu, H.Y., Dai, L.D., Li, H.P., Hui, K.S., and Sun, W.Q. (2017) Influence of dehydration on the electrical conductivity of epidote and implications for high-conductivity anomalies in subduction zones. *Journal of Geophysical Research: Solid Earth*, 122, 2751–2762.
- Hu, H.Y., Dai, L.D., Li, H.P., Sun, W.Q., and Li, B.S. (2018) Effect of dehydrogenation on the electrical conductivity of Fe-bearing amphibole: Implications for high conductivity anomalies in subduction zones and continental crust. *Earth and Planetary Science Letters*, 498, 27–37.
- Hwang, H., Seoung, D., Lee, Y., Liu, Z.X., Liermann, H.P., Cynn, H., Vogt, T., Kao, C.C., and Mao, H.K. (2017) A role for subducted super-hydrated kaolinite in Earth's deep water cycle. *Nature Geoscience*, 10, 947–953.
- Johnston, C.T., Wang, S.L., Bish, D.L., Dera, P., Agnew, S.F., and Kenney, J.W. (2002) Novel pressure-induced phase transformations in hydrous layered materials. *Geophysical Research Letters*, 29, 17–17–4.
- Kozik, T., Trnovcová, V., Mariani, E., Štubňa, I., and Rohác, J. (1992) The temperature dependence of the electric conductivity of unfired porcelain mixture. *Ceramics—Silikáty*, 36, 69–72.
- Kubliha, M., Trnovcová, V., Ondruška, J., Štubňa, I., Bošák, O., and Kaljuvee, T. (2017) Comparison of dehydration in kaolin and illite using DC conductivity measurements. *Applied Clay Science*, 149, 8–12.
- Laiglesia, A. (1993) Pressure induced disorder in kaolinite. *Clay Minerals*, 28, 311–319.
- Mercier, P.H.J., and Le Page, Y. (2009) Ab initio exploration of layer slipping transformations in kaolinite up to 60 GPa. *Materials Science and Technology*, 25, 437–442.
- Mercier, P.H.J., Le Page, Y., and Desgreniers, S. (2010) Kaolin polytypes revisited ab initio at 10 GPa. *American Mineralogist*, 95, 1117–1120.
- Ono, S. (1998) Stability limits of hydrous minerals in sediment and mid-ocean ridge basalt compositions: Implications for water transport in subduction zones. *Journal of Geophysical Research: Solid Earth*, 103, 18,253–18,267.
- Samyn, P., Schoukens, G., and Stanssens, D. (2015) Kaolinite nanocomposite platelets synthesized by intercalation and imidization of poly(styrene-co-maleic anhydride). *Materials*, 8, 4363–4388.
- Schroeder, P.A., and Erickson, G. (2014) Kaolin: From ancient porcelains to nanocomposites. *Elements*, 10, 177–182.
- Sun, W.Q., Dai, L.D., Li, H.P., Hu, H.Y., Wu, L., and Jiang, J.J. (2017) Electrical conductivity of mudstone (before and after dehydration at high *P-T*) and a test of high conductivity layers in the crust. *American Mineralogist*, 102, 2450–2456.
- Trnovcová, V., Furár, I., and Hanic, F. (2007) Influence of technological texture on electrical properties of industrial ceramics. *Journal of Physics and Chemistry of Solids*, 68, 1135–1139.
- Welch, M.D., and Crichton, W.A. (2010) Pressure-induced transformations in kaolinite. *American Mineralogist*, 95, 651–654.
- Welch, M.D., Montgomery, W., Balan, E., and Lerch, P. (2012) Insights into the high-pressure behavior of kaolinite from infrared spectroscopy and quantum-mechanical calculations. *Physics and Chemistry of Minerals*, 39, 143–151.
- Windom, H.L. (1976) Lithogenous material in marine sediments. *Chemical Oceanography*, 5, 103–135.
- Yang, L.F., Jiang, J.J., Dai, L.D., Hu, H.Y., Hong, M.L., Zhang, X.Y., Li, H.P., and Liu, P.F. (2021) High-pressure structural phase transition and metallization in Ga<sub>2</sub>S<sub>3</sub> under non-hydrostatic and hydrostatic conditions up to 36.4 GPa. *Journal of Materials Chemistry C*, 9, 2912–2918.
- Zhang, Y.D., Liu, Q.F., Xiang, J.J., Zhang, S.L., and Frost, R.L. (2014) Insight into morphology and structure of different particle sized kaolinites with same origin. *Journal of Colloid and Interface Science*, 426, 99–106.
- Zhuang, Y.K., Dai, L.D., Wu, L., Li, H.P., Hu, H.Y., Liu, K.X., Yang, L.F., and Pu, C. (2017) Pressure-induced permanent metallization with reversible structural transition in molybdenum disulfide. *Applied Physics Letters*, 110, 122103.

MANUSCRIPT RECEIVED OCTOBER 20, 2020

MANUSCRIPT ACCEPTED MAY 27, 2021

MANUSCRIPT HANDLED BY JIANWEI WANG

#### Endnote:

<sup>1</sup>Deposit item AM-22-37863, Online Materials. Deposit items are free to all readers and found on the MSA website, via the specific issue's Table of Contents (go to [http://www.minsocam.org/MSA/AmMin/TOC/2022/Mar2022\\_data/Mar2022\\_data.html](http://www.minsocam.org/MSA/AmMin/TOC/2022/Mar2022_data/Mar2022_data.html)).